Cold gas in distant galaxies

Boogaard, L.A.

Cover Page

Universiteit Leiden

Leiden University
Repository

The handle http://hdl.handle.net/1887/3147175 holds various files of this Leiden University dissertation.

Author: Boogaard, L.A.
Title: Cold gas in distant galaxies
Issue date: 2021-02-25

5 | The ALMA Spectroscopic Survey in the HUDF: Multiband constraints on line-luminosity functions and the cosmic density of molecular gas

Abstract

We present a CO and atomic fine-structure line-luminosity function analysis using the ALMA Spectroscopic Survey in the *Hubble* Ultra Deep Field (ASPECS). ASPECS consists of two spatially overlapping mosaics that cover the entire ALMA 3 mm and 1.2 mm bands. We combine the results of a line-candidate search of the 1.2 mm data cube with those previously obtained from the 3 mm cube. Our analysis shows that $\sim$ 80% of the line flux observed at 3 mm arises from CO(2−1) or CO(3−2) emitters at $z = 1 − 3$ ('cosmic noon'). At 1.2 mm, more than half of the line flux arises from intermediate-J CO transitions ($J_{up} = 3 − 6$); $\sim$ 12% from neutral carbon lines; and < 1% from singly-ionized carbon, [C II]. This implies that future [C II] intensity mapping surveys in the epoch of reionization will need to account for a highly significant CO foreground. The CO luminosity functions probed at 1.2 mm show a decrease in the number density at a given line luminosity (in units of L') at increasing J_{up} and redshift. Comparisons between the CO luminosity functions for different CO transitions at a fixed redshift reveal subthermal conditions on average in galaxies up to $z \sim 4$. In addition, the comparison of the CO luminosity functions for the same transition at different redshifts reveals that the evolution is not driven by excitation. The cosmic density of molecular gas in galaxies, ρ_{H_2}, shows a redshift evolution with an increase from high redshift up to $z \sim 1.5$ followed by a factor $\sim$ 6 drop down to the present day. This is in qualitative agreement with the evolution of the cosmic star formation rate density, suggesting that the molecular gas depletion time is approximately constant with redshift, after averaging over the star-forming galaxy population.

R. Decarli, M. Aravena, L. A. Boogaard, C. Carilli, J. González-López, F. Walter, *et al.*

5.1   Introduction

Stars form in the dense, molecular phase of the interstellar medium (ISM; see, e.g., reviews in Kennicutt & Evans 2012, Carilli & Walter 2013, Dobbs et al. 2014, Combes 2018, Tacconi et al. 2020, and Hodge & da Cunha 2020). Molecular gas is thus a key ingredient of galaxy formation, and it plays a critical role in shaping the history of cosmic star formation (e.g., Lilly et al., 1995; Madau et al., 1996; Hopkins & Beacom, 2006; Madau & Dickinson, 2014). Gauging the amount of molecular gas in galaxies available for star formation, as well as its physical conditions and excitation properties, is thus pivotal in our understanding of the formation and evolution of galaxies. For instance, the cosmic star formation rate density, ρ_{SFR}, may result from an evolution of the amount of molecular gas stored in galaxies, averaged over cosmological volume, ρ_{H_2}, or from an evolution in the efficiency at which molecular gas is converted into stars (as set by the inverse of the depletion time, t_{dep}, i.e., the timescale required for the galaxy to exhaust its current gaseous reservoirs, under the assumption that stars keep forming at the current rate), or by a combination of both.

Molecular hydrogen, H_2, is a poor radiator (e.g., Omont, 2007); therefore, observations of the molecular phase of the ISM typically rely on other molecules, in particular the carbon monoxide, $^{12}C^{16}O$ (hereafter, CO), which is abundant in the star-forming ISM and efficiently radiates via rotational transitions even at modest excitation energies (corresponding to excitation temperatures of a few tens of K, as observed in the cold, star-forming medium). Low-J CO transitions ($J_{\mathrm{up}} \lesssim 4$) have rest-frame frequencies, ν_0, of 100–500 GHz (rest wavelength $\lambda_0 = 0.6\,\mathrm{mm}$–3 mm), and are often used to gauge the mass in molecular gas, as their luminosity is only modestly dependent on the gas physics (in particular, excitation temperature and density). Intermediate-J CO transitions ($5 \lesssim J_{\mathrm{up}} \lesssim 7$; $\nu_0 = 500-900\,\mathrm{GHz}$, $\lambda_0 = 0.3-0.6\,\mathrm{mm}$) and high-$J$ CO transitions ($J_{\mathrm{up}} \gtrsim 8$, $\nu_0 > 900\,\mathrm{GHz}$), on the other hand, owe their luminosity to the higher excitation, warmer or denser medium—thus they are better tracers of starbursting activity, nuclear activity, or shocks (see discussions in, e.g., Weiss et al., 2007a; Carilli & Walter, 2013; Daddi et al., 2015; Kamenetzky et al., 2018; Boogaard et al., 2020).

Surveys of molecular gas in high-redshift galaxies are blossoming thanks to the unprecedented observational capabilities offered by the Jansky Very Large Array (VLA), the IRAM NOrthern Expanded Millimeter Array (NOEMA), and the Atacama Large Millimeter Array (ALMA). The number of CO-detected galaxies at $z > 0.5$ has increased significantly in the last few years, and now exceeds 250 (see, e.g., the compilation in Tacconi et al., 2018). Most of these detections come from targeted investigations, i.e., investigations of the molecular content of known galaxies preselected based on their redshift, stellar mass, far-infrared luminosity, star formation rate (SFR), nuclear activity, apparent luminosity, etc. These studies have been instrumental in effectively establishing empirical relations between gas content and a number of galaxy properties (e.g., Greve et al., 2005; Daddi et al., 2010b; Tacconi et al., 2010, 2013, 2018; Aravena et al., 2012; Genzel et al., 2010, 2011, 2015; Bothwell et al., 2013; Dessauges-Zavadsky et al., 2017).

Molecular scans, i.e., interferometric observations of blank fields over a wide frequency range at millimeter wavelengths, represent a powerful complementary approach. By searching for molecular gas emission irrespective of the position and redshift, they effectively result in

a line flux-limited survey of a well-defined cosmological volume, and do not depend on any preselection. The first molecular scan that reached sufficient depth to secure CO detections in typical galaxies at $z > 1$ came from a > 100-hr long campaign targeting a ~ 1 arcmin^2 region of the *Hubble* Deep Field North (Williams et al., 1996) in the 3 mm band using the IRAM/Plateau de Bure Interferometer (PdBI; Walter et al., 2012, 2014; Decarli et al., 2014). The ALMA Spectroscopic Survey in the *Hubble* Ultra Deep Field, ASPECS, built on the success of the PdBI program by performing two frequency scans at 3 mm and 1.2 mm. The ASPECS-Pilot program (Walter et al., 2016; Aravena et al., 2016b,c; Decarli et al., 2016a,b; J. Bouwens et al., 2016; Carilli et al., 2016) offered a first glimpse at the molecular gas content in galaxies residing in one of the best-studied regions of the extragalactic sky, the *Hubble* Ultra Deep Field (Beckwith et al., 2006). The ASPECS-Pilot survey was then expanded into an ALMA Large Program (LP) targeting a 4.6 arcmin^2 area, with the same survey strategy (González-López et al., 2019, 2020; Decarli et al., 2019; Boogaard et al., 2019, 2020; Aravena et al., 2019, 2020; Popping et al., 2019, 2020; Uzgil et al., 2019; Magnelli et al., 2020; Inami et al., 2020; Walter et al., 2020). Among other results, ASPECS provided robust constraints on the low-J CO luminosity functions up to $z \sim 4$, and an estimate of the evolution of the cosmic density of molecular gas in galaxies, $\rho_{H_2}(z)$. A follow-up program dubbed VLASPECS used the NSF's Karl G. Jansky Very Large Array, VLA, to secure 30.6–38.7 GHz coverage over part of the ASPECS footprint, thus providing a low-J anchor to CO excitation models for galaxies by directly measuring CO(1–0) luminosities in the redshift range $z = 2.0 - 2.7$ (Riechers et al., 2020).

Other molecular scan efforts appeared in the literature in the last couple of years: The COLDz survey used > 320 hr of the VLA time to sample CO(1–0) emission at $z \approx 2 - 3$ ('cosmic noon') as well as CO(2–1) at $z \approx 5 - 7$ over ~ 60 arcmin^2 in parts of the COSMOS (Scoville et al., 2007) and GOODS-North (Giavalisco et al., 2004) fields (Pavesi et al., 2018; Riechers et al., 2019, 2020). Lenkić et al. (2020) used the Plateau de Bure High-z Blue-Sequence Survey 2 (PHIBSS2) data (Tacconi et al., 2018) to search for serendipitous emission in the cubes, besides the central targets. These studies place first direct constraints on the CO luminosity function in galaxies at $z \sim 2$, and revealed a higher molecular content in galaxies at these redshifts compared to the local universe: $\rho_{H_2}(z = 2 - 3) \approx (1 - 20) \times 10^7 \, M_\odot \, Mpc^{-3}$. A few serendipitous molecular line detections have been reported in the the fields of sub-millimeter galaxies (Wardlow et al., 2018; Cooke et al., 2018), in an ALMA deep field around SSA22 (Hayatsu et al., 2017) and around graviational lensing clusters (Yamaguchi et al., 2017; González-López et al., 2017b). Finally, Klitsch et al. (2019) used the high signal-to-noise ratio (S/N) of mm-bright calibrators in the ALMA archive to search for CO absorption features. They do not detect any extragalactic source, which sets constraints on both the CO luminosity functions and $\rho_{H_2}(z)$ up to $z \sim 1.7$. In addition to CO-based estimates, various studies have inferred molecular gas mass functions and $\rho_{H_2}(z)$ via estimates based on the dust continuum, but this relies on an empirically-calibrated gas-to-dust conversion (e.g., Scoville et al., 2017; Liu et al., 2019; Magnelli et al., 2020).

In this paper, we capitalize on the completed ASPECS dataset in order to constrain the luminosity functions and average cosmic content of molecular gas in galaxies throughout cosmic time. First, we present the new 1.2 mm dataset (§ 5.2.1), the ancillary data (§ 5.2.2), and the approach adopted in the analysis (§ 5.3). Then, we complement the 1.2 mm dataset
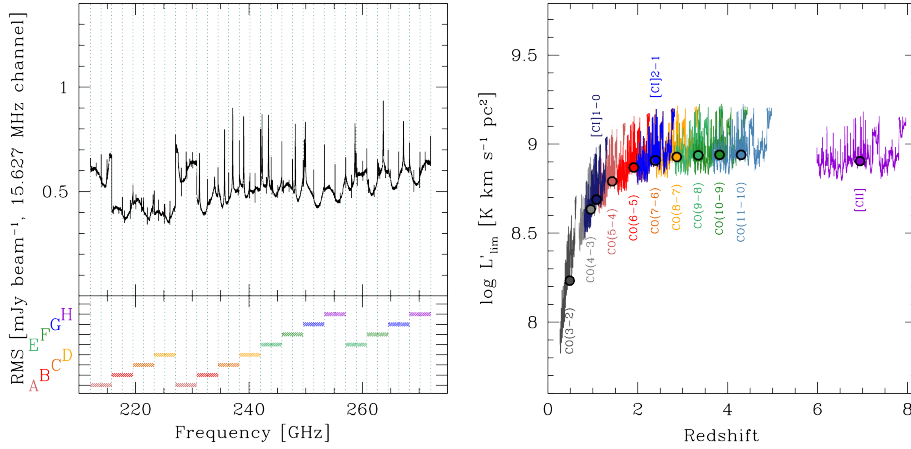
Figure 5.1: Sensitivity limits of the ASPECS 1.2 mm cube. *Left:* Channel rms as a function of frequency. For a 15.6 MHz channel, the typical rms is ~ 0.5 mJy beam^{-1} throughout the entire band. The frequency settings used in the observations (labeled A–H) and the edges of each spectral window are also marked. *Right:* Line-luminosity limits (in units of K km s^{-1} pc^2) as a function of redshift. Here we assume a 5σ limit for a line width of 200 km s^{-1}. The dots highlight the fiducial limit, obtained as the median sensitivity throughout the band.

with the information from the 3 mm part of ASPECS in a homogeneous analysis of molecular and atomic line emission from the cold ISM in high-redshift galaxies (§ 5.4). We present our conclusions in § 5.5. Throughout this paper we adopt a ΛCDM cosmological model with $H_0 = 70$ km s^{-1} Mpc^{-1}, $\Omega_m = 0.3$ and $\Omega_\Lambda = 0.7$ (consistent with the measurements by the Planck Collaboration et al., 2016).

5.2   Observations

5.2.1   ALMA data

The ASPECS LP survey is an ALMA Cycle 4 Large Program comprising two bands, at 3 mm and 1.2 mm. The former is presented and discussed elsewhere (González-López et al., 2019; Decarli et al., 2019; Boogaard et al., 2019; Aravena et al., 2019; Popping et al., 2019; Uzgil et al., 2019; Inami et al., 2020). The latter consists of a mosaic of 85 pointings in the eXtremely Deep Field (XDF, Illingworth et al. 2013; also dubbed *Hubble* Deep Field 2012 or HUDF12, Koekemoer et al. 2013) for a total area of 4.2 arcmin^2 down to 10% sensitivity, or 2.9 arcmin^2 within the 50% primary beam response. The observing strategy involves covering the full mosaic area at each telescope visit. The pointings were arranged in classical hexagonal patterns at 11$''$ separation, which ensures Nyquist sampling throughout the entire frequency range of the observations and results in a spatially-uniform sensitivity throughout the majority of the footprint.

Table 5.1: Emission lines, corresponding redshift bins, volume-weighted average redshift, cosmic volume (in comoving units, within the area of $> 50\%$ sensitivity), and typical 5σ line-luminosity limit at $\langle z \rangle$, assuming a line width of $200\,\mathrm{km\,s^{-1}}$ in ASPECS LP 1.2 mm (observed range: 212–272 GHz).

Line	Redshift	$\langle z \rangle$	Volume (Mpc^3)	limit L ($10^7\,L_\odot$)	limit L' ($10^8\,\mathrm{K\,km\,s^{-1}\,pc^2}$)
(1)	(2)	(3)	(4)	(5)	(6)
CO(3–2)	0.2711–0.6306	0.49	921.3	0.023	1.710
CO(4–3)	0.6947–1.1740	0.96	2960.9	0.135	4.299
CO(5–4)	1.1183–1.7173	1.43	5106.3	0.378	6.174
CO(6–5)	1.5418–2.2606	1.91	6923.8	0.781	7.384
CO(7–6)	1.9651–2.8037	2.39	8470.4	1.358	8.088
CO(8–7)	2.3884–3.3467	2.87	9597.2	2.121	8.464
CO(9–8)	2.8115–3.8895	3.35	10478.0	3.085	8.647
CO(10–9)	3.2345–4.4321	3.82	11012.3	4.262	8.712
CO(11–10)	3.6574–4.9745	4.30	11371.6	5.660	8.696
[C I]$_{1-0}$	0.8091–1.3207	1.08	3540.8	0.186	4.878
[C I]$_{2-1}$	1.9750–2.8164	2.40	8509.3	1.374	8.102
[C II]	5.9861–7.9619	6.94	12621.6	17.61	8.018

Observations were carried out in two parts, a first pass in 2017, March–April (roughly 20% of the total data volume spread among all of the requested frequency settings) and the remainder in 2018, May–July. The 2017 observations were collected with average weather conditions, with precipitable water vapour 2.5–3.0 mm; on the other hand, the 2018 observations were gathered in excellent weather conditions, with precipitable water vapour ~ 0.6 mm in most of the executions. The array was in compact, C40-1 or C40-2 configurations, with baselines in the range 15 m–320 m.

The observations sampled eight different frequency tunings, continuously encompassing the entire 212–272 GHz window (see Figure 5.1). Quasars J0329–2357, J0334–4008, J0348–2749, and J0522–3627 were employed as pointing, phase, amplitude, and bandpass calibrators.

We processed the raw data using the CASA calibration pipeline for ALMA (v.5.1.1; see McMullin et al., 2007). No additional flagging was applied. We inverted the visibilities using the task tclean, and adopting natural weighting. The resulting beam is $\sim 1.5'' \times 1.1''$. Along the spectral axis, the cube was resampled using 15.627 MHz wide channels ($\approx 19\,\mathrm{km\,s^{-1}}$ at 242 GHz). Cleaning was performed down to 2σ per channel after putting cleaning boxes on all the sources with S/N > 5 in their continuum emission. We reach a sensitivity of ~ 0.5 mJy beam^{-1} per 15.627 MHz channel roughly constant throughout the 1.2 mm band (see Figure 5.1). We also created a continuum-subtracted version of the cube, after identifying and excluding the channels with the brightest emission lines (see González-López et al. 2020 for details). Finally, we created a tapered version of the cube, where we degrade the angular resolution by setting the restoringbeam=2'' in the task tclean. We use this tapered cube to extract 1D spectra of the detected galaxies, following González-López et al. (2019).

5.2.2   Ancillary data

The targeted field lies in the *Hubble* Ultra Deep Field (HUDF), arguably the best studied extragalactic field in the sky. We employ the 3D-*HST* photometric catalog by Skelton et al. (2014), which relies on optical *Hubble*/Advanced Camera for Surveys data (Beckwith et al., 2006), deep near-infrared *Hubble*/Wide Field Camera 3 observations from the Cosmic Assembly Near-infrared Deep Extragalactic Legacy Survey (CANDELS; Grogin et al. 2011; Koekemoer et al. 2011), enriched with multiwavelength photometry and spectroscopy from various surveys (see Boogaard et al., 2019, and references therein). In particular, the MUSE *Hubble* Ultra Deep Survey (Bacon et al., 2017) provides integral field spectroscopy of a $3' \times 3'$ field (encompassing the whole HUDF) over the wavelength range 4750–9300 Å. More than 1500 galaxies have secured redshifts from MUSE (Inami et al., 2017), ~ 700 of which are within the area of the ASPECS LP 1.2 mm mosaic with >50% primary beam response.

When comparing ALMA observations to other catalogs, we account for a known systematic astrometry offset (ΔRA = +0.076$''$, ΔDec = −0.279$''$) between optical and mm/radio data (Rujopakarn et al., 2016; Dunlop et al., 2017).

# 5.3   Analysis and Results

5.3.1   Line search at 1.2 mm

We search for emission lines in the original and the continuum-subtracted ASPECS LP 1.2 mm cubes using FINDCLUMPS (Walter et al., 2016; Decarli et al., 2019; González-López et al., 2019). The code performs a floating average of channels over various kernel widths (with one channel corresponding to $\approx 19 \, \mathrm{km \, s^{-1}}$ at the center of the bandwidth). Each averaged channel is searched for both positive and negative peaks. The S/N of a line candidate is computed as the ratio between the flux density measured at the centroid of the line candidate and the rms of the map used in the line identification. We refer to the line search results from the continuum-subtracted cube for line candidates that lie within 2$''$ from a bright continuum source from the compilation in González-López et al. (2020), and to the results from the original cube for anywhere else in the mosaic.

Positive peaks are a combination of signal from astrophysical sources and noise, while negative peaks are only due to noise. The latter are thus used to statistically infer the reliability or 'fidelity' of a line candidate, given its width (σ_{line}) and signal to noise (S/N):

$$\mathrm{Fidelity(S/N}, \sigma_{\mathrm{line}}) = 1 - \frac{N_{\mathrm{neg}}(\mathrm{S/N}, \sigma_{\mathrm{line}})}{N_{\mathrm{pos}}(\mathrm{S/N}, \sigma_{\mathrm{line}})} \qquad (5.1)$$

where $N_{\mathrm{pos,neg}}$ is the number of line candidates in a given S/N and σ_{line} bin. Only S/N > 4 line candidates are considered in this analysis. For each line width bin, we fit the observed distribution of the noise peaks with the tails of a Gaussian function centered at zero, and the additional signal due to real sources as a power law. The fit is performed in two steps, first by modeling the negative distributions in σ_{line} bins, then by fitting the positive distributions capitalizing on the posterior parameters of the negative fits for the noise component of the
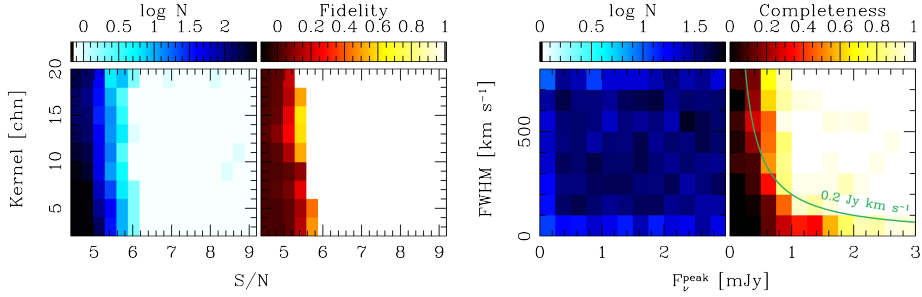
Figure 5.2: *First panel:* Number of observed (positive) line candidates from the line search as a function of S/N and kernel width that maximized the S/N of the line candidate in the line search. *Second panel:* Best fits of the fidelity dependence on S/N and kernel width. The fidelity of line candidate is close to unity at S/N > 5.8, and drops rapidly to zero at S/N < 5. The fidelity at a given S/N increases with increasing line widths, as expected because of the fewer independent noise realizations in the cubes. *Third panel:* Number of simulated lines injected in the cube for completeness assessments, as a function of line peak flux, F_{ν}^{peak}, and width (parametrized as FWHM). Only lines located within the footprint at > 50% response in the cube. *Fourth panel:* Completeness of the line search. The completeness is $\gtrsim 90\%$ for virtually any line with integrated flux larger than 0.2 Jy km s^{-1} (indicated by a green solid line) and peak fluxes of > 1 mJy.

observed distributions. This allows us to mitigate limitations due to the low number of entries in some bins, while properly accounting for their statistical relevance. Following Pavesi et al. (2018), González-López et al. (2019), and Decarli et al. (2019), we conservatively treat these estimates of the fidelity as upper limits; e.g., in each realization of the luminosity functions, a line with a fidelity of 40% has up to 40% chance to be used in the analysis. The upper-right panel of Figure 5.2 show the behaviour of the fidelity as a function of the adopted kernel width (i.e., the number of channels that maximizes the S/N of a line candidates—this is a proxy of the line width) as well as of the integrated S/N of the line candidate. The fidelity is close to 100% for any line at S/N > 6, and drops rapidly to zero between S/N = 5 − 6, with narrower lines being typically less reliable than broader lines with the similar total S/N. We refer the reader to Decarli et al. (2019) and González-López et al. (2019) for detailed discussions on the assessment of the line reliability. Finally, we adopt a fidelity of unity (not treated as an upper limit) for the high-significance line candidates associated with known sources for which we have clear 1.2 mm continuum counterparts, as well as a spectroscopic redshift from MUSE or from our 3 mm line search. These sources are studied in detail in Boogaard et al. (2020) and Aravena et al. (2020). The final catalog from the line search consists of 234 line candidates with fidelity > 0.2, 75 with fidelity > 0.5, and 35 with fidelity > 0.8.

We estimate the completeness by injecting simulated emission lines with a range of input parameters into the observed data cube. We adopt a 3D Gaussian profile for mock lines. In the spatial dimension, we assume the position angle and width of the major and minor axes of the synthesized beam (i.e., sources are spatially unresolved). We run the line search on the cube, and then define the completeness as a function of the input line parameters

as the ratio between the number of retrieved versus injected sources. As input parameters, we consider the right ascension, α; the declination, δ; the observed frequency, ν_{obs}; the line width along the spectral axis, $FWHM = 2\sqrt{2 \ln 2}\,\sigma_{line}$; the line peak intensity, F_ν^{peak}. Sources are distributed uniformly in the sampled parameter space (corresponding to the actual 3D coverage of ASPECS LP 1.2 mm mosaic in terms of α, δ, and ν_{obs}; and ranging between 0–800 km s^{-1} and 0–3 mJy in terms of FWHM and F_ν^{peak}). A total of 8000 mock lines were injected, > 3000 of which reside within the area with $> 50\%$ primary beam response. The bottom panels of Figure 5.2 show the number of injected lines as a function of FWHM and F_ν^{peak}, and the associated completeness in bins of 100 km s^{-1} and 0.25 mJy in line width and peak flux. The other free parameters in our simulation do not appear to significantly affect the completeness of the line search (after accounting for the primary beam response). We drop all line candidates with a completeness of < 0.2 from our analysis. The median correction due to completeness is $< 30\%$.

5.3.2   Line fluxes

For each line candidate, we extract a 1-D spectrum from the pixel where the line spatial centroid is found. We then fit the extracted spectrum with a continuum and a Gaussian profile, using our custom Bayesian Monte Carlo Markov Chain procedure, using FINDCLUMPS results as priors (see Decarli et al., 2019).

   As we push our search towards the detection limit of our survey, we might tend to preferentially pick sources that appear brighter than they are due to noise fluctuations. We investigate the impact of flux boosting by comparing the injected and recovered fluxes of mock lines (see § 5.3.1 for details on the line simulations). Figure 5.3 compares the measured versus injected fluxes as a function of the detection S/N. The measured flux is typically within 30% of the input flux (at 1σ) in the $4.5 < S/N < 7$ regime. Flux boosting appears to be significant (i.e., the recovered flux exceeds 3σ of the distribution width)[40] in $\approx 10\%$ of sources with S/N < 5, and $\sim 1\%$ of the sources at S/N > 6. Because of the modest fidelity of sources with S/N < 5.8, we consider flux boosting negligible for the purpose of our analysis.

5.3.3   Line identification and redshifts

Sources with a near-infrared counterpart

Table 5.1 lists the transitions we are sensitive to, in various redshift bins.[41] In order to identify the rest-frame transition associated with a given line candidate, we first cross-match our line candidate compilation with catalogs from ancillary data (see § 5.2.2). All the entries in our galaxy catalog have a redshift estimate (with a wide range of accuracy, from very high for MUSE-identified sources with several bright emission lines to very poor for faint, photometric dropouts detected only in a handful of broad band filters). For each line candidate,

---

[40]The impact of flux boosting is likely larger for spatially-extended sources (see, e.g. Pavesi et al., 2018). However, our analysis assumes unresolved emission in the tapered cube for all of the sources.

[41]The ASPECS LP 1.2 mm coverage formally includes also the CO(2–1) transition at $z < 0.0874$. However, the sampled volume within this redshift range is $\sim 3.9 \times 10^{-4}$ Mpc^3, insufficient for this analysis.
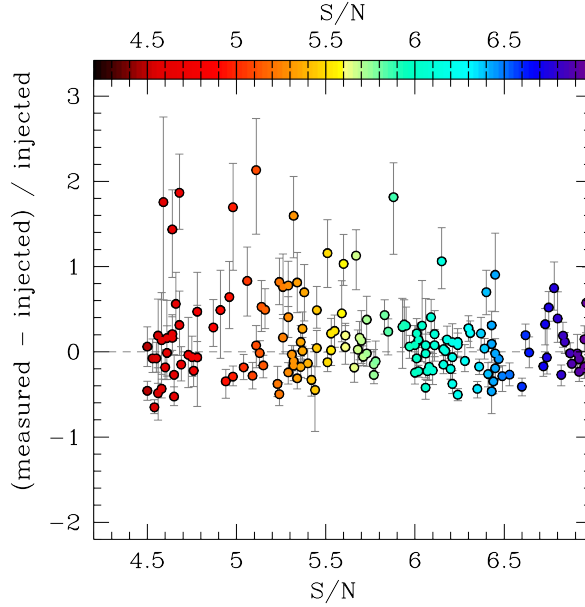
Figure 5.3: The impact of flux boosting on our analysis, estimated by comparing the injected and measured fluxes of mock lines. Small symbols show a random subset of individual mock lines, larger symbols are median values in bins of $\Delta S/N = 0.5$. Flux boosting affects the flux measurement of $\approx 10\%$ of lines at $S/N < 5$, and is completely negligible at $S/N > 6$.

we consider as potential counterpart sources within $1''$ from the line spatial centroid. We identify the transition as the one that would yield the closest line redshift, z_{line}, to the one reported in the ancillary catalog, z_{cat}. We consider good matches line candidates that are found within $1''$ from a known optical/near-infrared counterpart, and with a redshift separation of $|\delta z| = |z_{\text{cat}} - z_{\text{line}}|/(1 + z_{\text{line}}) < 0.1$ (0.01 for sources with a spectroscopic redshift). All of the fidelity > 0.8 lines in the search have a clear counterpart (see Figure 5.4).

Ignoring the effects of gravitational lensing, we can estimate the impact of chance associations (i.e., the probability of intersecting a galaxy at a random point in our datacube) as:

$$P(\text{chance}) = \sum_i \frac{A_{\text{beam}}}{A_{\text{footprint}}} \frac{2\sigma_z}{(1 + z)\Delta z_i} \tag{5.2}$$

where A_{beam} and $A_{\text{footprint}}$ are the areas of the synthesized beam and of the ASPECS LP 1.2 mm footprint, respectively; σ_z is the uncertainty in the redshift, which we assume to be 0.1; Δz_i is the redshift coverage of ASPECS LP 1.2 mm in transition i; and the index i runs through the various transitions considered in our analysis. After summing over all of the transitions, we find that the probability of chance association is $\sim 4.3\%$, i.e., from all the line candidates with a counterpart entering our analysis, only a handful of chance associations are expected (and virtually zero if one considers spectroscopic redshift uncertainties instead).
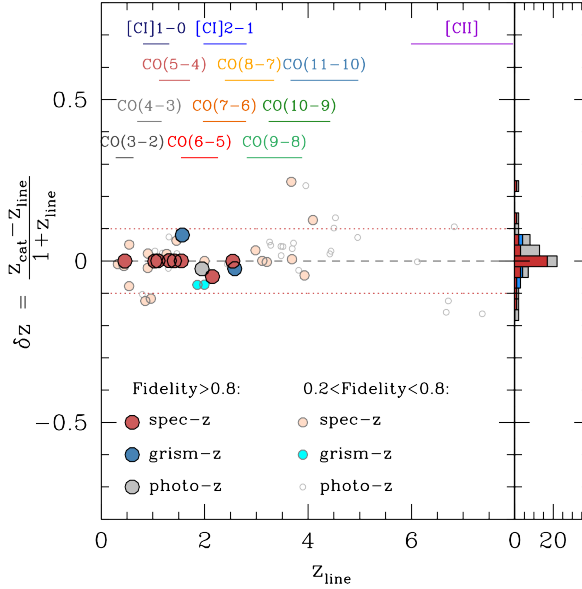
Figure 5.4: Redshift match from the line search in the ASPECS LP 1.2 mm mosaic, z_{line}, and the ancillary catalog values, z_{cat}, based on the 3D-HST catalog (Skelton et al., 2014), augmented with the most up to date spectroscopic information (see § 5.2.2 for details). We consider good matches cases where $|\delta z| < 0.1$ (< 0.01 for sources with spectroscopic redshifts). All of the high fidelity lines have a matching redshift in the catalog. The redshift ranges mapped by the various transitions considered in this work are marked as horizontal bars.

Figure 5.5 shows a pie chart of the fidelity-corrected total flux of all the line candidates with an optical/near-infrared counterpart and with fidelity > 0.5. The 3 mm flux distribution is dominated by CO(2–1) (53%) and CO(3–2) (27%), observed at $z = 1 − 3$, while higher-J lines contribute progressively less [CO(4–3): 10%; CO(5–4): 7%; CO(6–5): 3%]. On the other hand, more than half of the total flux measured in lines (62%) in the ASPECS LP 1.2 mm mosaic comes from intermediate-J CO transitions ($3 \leq J_{up} \leq 6$); 25% arises from higher-J CO transitions; 12% from [C I]; and less than 1% from [C II]. The uncertainties on these fractions are of ~ 25% for the CO lines, and ~ 50% for the carbon lines, as estimated from the Poissonian uncertainties. The fact that the contribution of [C II] flux to the total line flux is < 1% in band 6 implies significant challenges for intensity mapping experiments of [C II] emission in the epoch of reionization (e.g., Crites et al., 2014; Lagache et al., 2018; Sun et al., 2018; Yue et al., 2015; Yue & Ferrara, 2019; Chung et al., 2020) as the signal will be dominated by CO foreground emission.
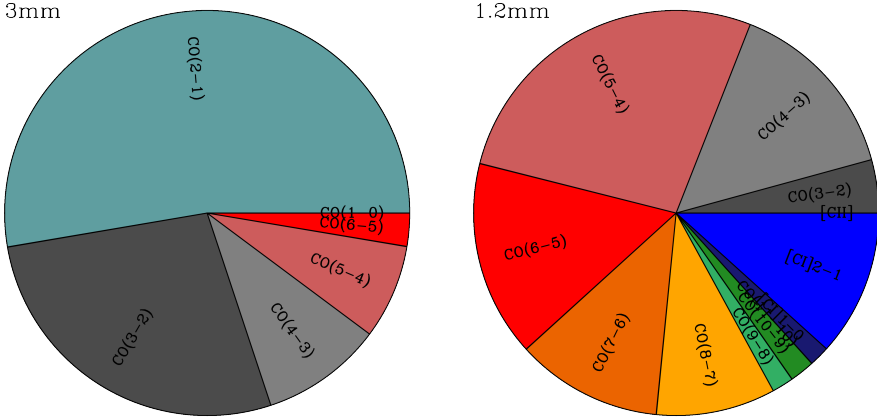
Figure 5.5: Pie charts of the fidelity-corrected flux distribution of the lines detected in the ASPECS LP 3 mm (*left*) and 1.2 mm (*right*) cubes. The 3 mm cube is dominated by low-J CO transitions observed at $z = 1 - 3$. At 1.2 mm, about 62% of the total line emission arises from CO transitions with intermediate $J = 3 - 6$. Higher-J transitions account for 25% of the total line flux in the 1.2 mm band. The two [C I] lines account for $\sim$ 12% of the total line emission, while [C II] contributes < 1%.

Sources without a near-infrared counterpart

The identification of lines without an optical/near-infrared counterpart (roughly 1/3 of the line candidates with fidelity > 0.8) is done via a bootstrap approach, following, e.g., Decarli et al. (2019). Here we assume that the probability distribution of a line identification is proportional to the volume sampled in each transition, scaled by a weight set to be equal to $r_{J1} = (0.46, 0.25, 0.12, 0.04)$ for $J_{up} = (3, 4, 5, 6)$, and to 0.01, 0.05 and 0.003 for $J_{up} > 6$, [C I]$_{1-0}$ and [C I]$_{2-1}$, respectively. These weights have been derived from the average CO spectral energy distribution derived for the ASPECS sources by Boogaard et al. (2020). The weights for [C I] lines are defined based on a fiducial flux ratio between [C I] lines and neighboring CO transitions (see, e.g., Walter et al., 2011; Boogaard et al., 2020). Finally, we do not include [C II], based on the flux distribution shown in Figure 5.5 and the analyses presented in B. Uzgil, et al. (in prep.) and Loiacono et al. (2020). We discuss different choices of assigning CO transtions (i.e., redshifts) to sources with no near-infrared counterpart in § 5.C.

5.3.4   Line luminosities and molecular gas masses

Line fluxes are transformed into luminosities following, e.g., Carilli & Walter (2013):

$$\frac{L'}{K \, km \, s^{-1} \, pc^2} = \frac{3.257 \times 10^7}{1 + z} \frac{F_{line}}{Jy \, km \, s^{-1}} \left(\frac{\nu_0}{GHz}\right)^{-2} \left(\frac{D_L}{Mpc}\right)^2 \tag{5.3}$$
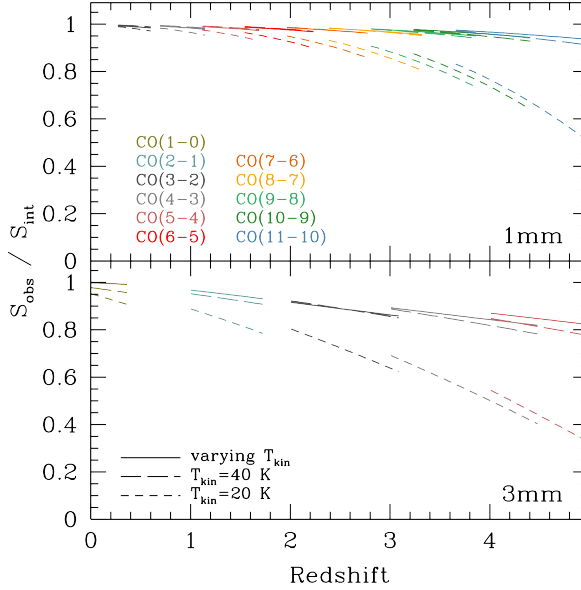
Figure 5.6: The effect of the CMB on the observed line fluxes. The correction is computed under the assumption of local thermal equilibrium, for different values of the gas kinetic temperature, $T_{kin} = 20$ K, 40 K, and for a redshift-dependent description as in Magnelli et al. (2014). The correction is always $\lesssim 20\%$ up to $z \sim 3$ for any $T_{kin} > 20$ K, and $< 10\%$ up to $z \sim 5$ for any $T_{kin} > 40$ K.

where F_{line} is the integrated line flux, ν_0 is the rest-frame frequency of the line, and D_L is the luminosity distance. We also compute line luminosities in solar units as:

$$\frac{L}{L_\odot} = \frac{1.04 \times 10^3}{1 + z} \frac{F_{line}}{Jy\,km\,s^{-1}} \frac{\nu_0}{GHz} \left(\frac{D_L}{Mpc}\right)^2. \tag{5.4}$$

As our observations probe the rest-frame far-infrared wavelengths of high-redshift galaxies, the Cosmic Microwave Background (CMB) might have an impact on the observed line fluxes. It provides an extra contribution to excitation temperature of the lines, but it also represents a background against which sources are observed. We follow the formalism presented in da Cunha et al. (2013) to compute the correction between the observed versus intrinsic line fluxes. The correction depends on the intrinsic excitation temperature in the gas. Here we assume local thermal equilibrium ($T_{kin} = T_{exc}$). Figure 5.6 shows the correction terms for two fixed temperature values $T_{kin} = 20, 40$ K, and for a redshift-dependent T_{kin} following the dust temperature evolution presented in Magnelli et al. (2014). We find that the correction is always $< 20\%$ for any temperature of interest $T_{kin} > 20$ K, up to $z \sim 3$, and $< 10\%$ for any $T_{kin} > 40$ K, for all the 1.2 mm CO lines. In Figure 5.6 we also show that the correction would be larger for lines observed at 3 mm, but still $< 20\%$ at any $z \lesssim 4$ for $T_{kin} = 40$ K. Because the exact correction depends on the (unknown) excitation temperature of the gas in our sources

and on the (unverified) validity of the local thermal equilibrium, and given how small the corrections are, we opt not to apply any CMB-related correction in the remainder of our analysis.

The lower-J CO transitions are converted into CO(1–0) luminosities by adopting the CO[J-(J-1)]-to-CO(1–0) luminosity ratios, r_{J1}, from the analysis of the CO excitation in CO-detected galaxies in ASPECS LP by Boogaard et al. (2020): L' [CO(1–0)] = L'/r_{J1}, with $r_{J1} = \{0.75\pm0.11, 0.46\pm0.07, 0.31\pm0.07\}$, for $J_{\text{up}} = \{2, 3, 4\}$. We also correct the results from ASPECS LP 3 mm (Decarli et al., 2019) accordingly for galaxies at $z < 2$. At higher redshifts, we adopt $r_{J1} = \{0.80 \pm 0.14, 0.61 \pm 0.13\}$, for $J_{\text{up}} = \{3, 4\}$. As discussed in Boogaard et al. (2020), the redshift dependence reflects the higher IR luminosity and IR surface brightness in the higher-redshift ASPECS LP sample (see also Aravena et al., 2020). We are consistent within uncertainties with the measurements of individual sources. As in Decarli et al. (2019), we include bootstrapped realizations of the uncertainties on r_{J1} in the conversion.

Finally, the CO(1–0) luminosities are converted into corresponding H_2 mass: $M_{H_2} = \alpha_{\text{CO}} L'_{\text{CO(1--0)}}$ (see Bolatto et al., 2013, for a review). The bulk of the flux emission in our observations arises from typical galaxies with close-to-solar metallicity (Boogaard et al., 2019; Aravena et al., 2019, 2020), for which a Galactic conversion factor should apply. Following the literature consensus, we adopt $\alpha_{\text{CO}} = 3.6\,M_\odot\,(\text{K km s}^{-1}\,\text{pc}^2)^{-1}$ (e.g., Daddi et al., 2010b). All the results based on α_{CO} would scale linearly if a different (but constant) value is adopted.

Atomic carbon transitions can also be used to infer constraints on the gas mass (see, e.g., Weiß et al., 2005; Walter et al., 2011; Alaghband-Zadeh et al., 2013; Bothwell et al., 2017; Popping et al., 2017b; Valentino et al., 2018). In the assumption of optically-thin line emission, the luminosity of the two [C I] transitions is related to the mass in neutral carbon as follows:

$$M_{[\text{C I}]}/M_\odot = 5.706 \times 10^{-4} \frac{Q_{\text{ex}}}{3} e^{23.6/T_{\text{ex}}} L'_{[\text{C I}]\,1-0} \qquad (5.5)$$

$$M_{[\text{C I}]}/M_\odot = 5.273 \times 10^{-3} \frac{Q_{\text{ex}}}{5} e^{62.5/T_{\text{ex}}} L'_{[\text{C I}]\,2-1} \qquad (5.6)$$

where $Q_{\text{ex}} = 1 + 3\,e^{-23.6/T_{\text{ex}}} + 5\,e^{-62.5/T_{\text{ex}}}$ is the partition function, T_{ex} is the excitation temperature in K, and line luminosities are quoted in units of K km s^{-1} pc^2. The mass estimates in Equation 5.5 and Equation 5.6 can be related to the molecular gas mass, under the assumption that all of the carbon is in neutral form. Assuming an abundance ratio [C I]/[H_2] = 1.9×10^{-5} (Boogaard et al. 2020, consistent with the $10^{-4.8\pm0.2}$ value reported by Valentino et al. 2018), we obtain $M_{H_2} = M_{[\text{C I}]}/(6\,[\text{C I}]/[H_2])$, where the factor of six accounts for the mass ratio between molecular Hydrogen and the carbon atom. In our analysis, we assume $T_{\text{ex}} = 29 \pm 6$ K (Walter et al., 2011).

The [C I] transitions have a number of advantages as molecular gas masses. In particular, $M_{[\text{C I}]}$ in Equation 5.5 is nearly linear with $L'_{[\text{C I}]\,1-0}$ for $T_{\text{ex}} \gtrsim 15$ K (a realistic scenario at high redshift), and optical depth is virtually never an issue once averaged over galactic scales. In principle, the mass estimates inferred via Equation 5.5 and Equation 5.6 are lower limits on M_{H_2}, because of the assumption that all of the carbon is in neutral form; however, the same assumption is usually at the root of the abundance estimates, i.e., the uncertainty cancels out. An additional caveat to consider is that, because [C I] is mostly optically thin, these [C I]-based

mass estimates are more sensitive to assumptions on carbon abundance and to the fraction of [C I] emitted from the neutral versus molecular medium than CO-based estimates.

5.3.5   Luminosity functions and ρ_{H_2}

In the construction of the CO luminosity functions, we follow the approach adopted in Decarli et al. (2019). Namely, we create 5000 realizations of the luminosity functions, folding in all of the uncertainties: formal flux measurement errors from the Gaussian fit, the uncertainties in the line identification (and the implications in terms of luminosity distance), the probability of a line to be spurious (as quantified via the fidelity), etc. In each realization, we keep only a subset of line candidates, based on their fidelity: We extract a number between 0 and 1 from a uniform distribution, and if the value is smaller than the line fidelity, we keep the line candidate in that realization. The resulting catalogs of lines are binned in luminosity, using 0.5 dex bins. Poissonian uncertainties are estimated for each bin, following Gehrels (1986). The number of entries and its uncertainties are then scaled to account for completeness and divided by the effective volume of the survey. Following Riechers et al. (2019) and Decarli et al. (2019), we create five versions of the luminosity functions, shifted by 0.1 dex one from the other, in order to expose the intra-bin variations despite the modest statistics in each bin. The luminosity functions (and their uncertainties) thus obtained are then averaged among all the realizations.

Figure 5.7 shows the resulting luminosity functions for each transition considered in this study: CO J_{up} = 1 to 4, and [C I]$_{1-0}$ from 3 mm, and CO J_{up} = 3 to 10, [C I]$_{1-0}$, [C I]$_{2-1}$, as well as [C II]. Tabulated values are reported in § 5.A. We limit our analysis to line candidates brighter than the formal 5σ limit (see Figure 5.1 and Table 5.1), and we only plot bins that are fully accommodated above this luminosity threshold and have an average of at least one entry throughout the realizations.

Finally, we convert the CO(1−0)−CO(4−3) line luminosities observed in either ASPECS band into H_2 masses as described in the previous subsection, we sum over the line candidates used in each realization of the luminosity function, and thus we infer the total molecular gas per cosmological volume, ρ_{H_2} (see Table 5.2). We remark that in the estimate of ρ_{H_2}, we do not extrapolate the LFs outside the observed line-luminosity ranges, but rather sum over the individual detections (corrected for fidelity and completeness).

5.4   Discussion

5.4.1   CO luminosity functions

Figure 5.7 shows the constraints on the luminosity functions for all the transitions covered in our analysis. Multiple lines are identified for all the mid-J CO transitions (up to J_{up} = 7). The CO(8−7) line is securely detected only in one case in the entire ASPECS volume. None of the higher-J CO lines is significantly detected individually, thus only low-fidelity candidates enter the luminosity function analysis for these transitions. Since our line-luminosity limit (in units of L') is rather flat with redshift at $z > 1$ (see Figure 5.1), this result per se can be
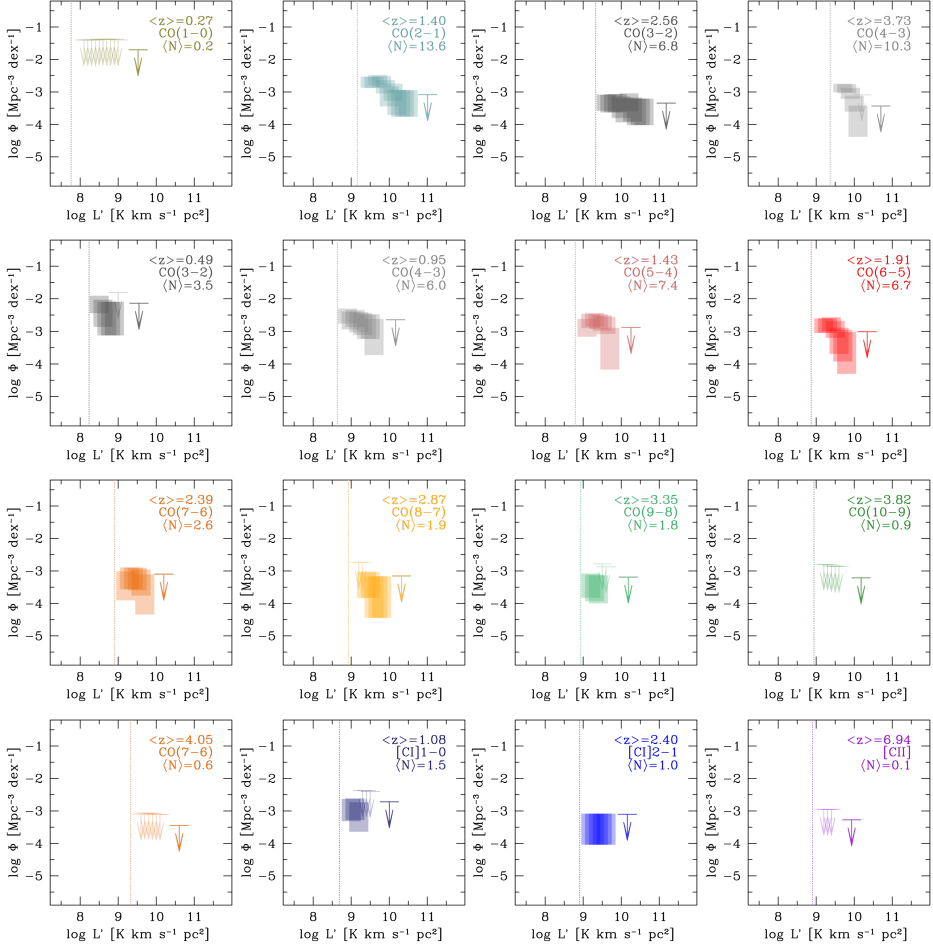
Figure 5.7: Constraints on the CO, [C I], and [C II] luminosity functions from ASPECS. The vertical extent of the boxes shows the average $\pm 1\sigma$ range in each 0.5 dex bin. For each transition, we report the volume-averaged redshift, and the average number of line candidates used in the various LF realizations. Bins with an average of > 1 line candidate entry per realization are shown as boxes, while arrows mark the corresponding 3σ limits for all of the other bins. The vertical bars show the formal 5σ line-luminosity limit (see Table 5.1).

Table 5.2: The cosmic molecular gas density (mass of molecular gas in galaxies per cosmological volume) as constrained by ASPECS.

| Redshift	ρ_{H_2}, 1σ $[10^7\,M_\odot\,\mathrm{Mpc}^{-3}]$	ρ_{H_2}, 2σ $[10^7\,M_\odot\,\mathrm{Mpc}^{-3}]$	Tracer
(1)	(2)	(3)	(4)
new from ASPECS LP 1.2 mm			
0.271–0.631	0.572–2.148	0.286–3.181	CO(3–2)
0.695–1.174	2.772–7.371	1.652–10.02	CO(4–3)
0.809–1.321	0.210–1.397	0.078–2.240	$[\mathrm{C\,I}]_{1-0}$
1.975–2.816	0.150–2.882	0.020–4.977	$[\mathrm{C\,I}]_{2-1}$
updated from ASPECS LP 3 mm			
0.003–0.369	0.015–0.281	0.002–0.485	CO(1–0)
1.006–1.738	4.053–7.489	2.953–9.462	CO(2–1)
2.008–3.107	1.844–4.438	1.164–6.007	CO(3–2)
3.011–4.475	1.686–3.289	1.193–4.220	CO(4–3)

attributed to subthermalized conditions in the ISM of typical galaxies at least at $J_{\mathrm{up}} \gtrsim 7$ or a drop in the gas masses or metallicities of galaxies at $z > 1$. In the following section we further explore these scenarios.

Same redshift, different CO transition

Figure 5.8 compares the CO luminosity function constraints from the two bands of ASPECS. At $\langle z \rangle \approx 1.43$, the ASPECS frequency coverage is such that we observe the CO(2–1) transition at 3 mm and the CO(5–4) transition at 1.2 mm. The inferred CO luminosity functions show an offset of about 0.5 dex in luminosity for a fixed number density. This immediately implies subthermalized conditions of the molecular ISM in the targeted galaxies ($r_{52} \lesssim 0.3$, consistent with the value of $r_{52} \approx 0.16$ derived by Boogaard et al. 2020).

Same CO transition, different redshifts

The ASPECS frequency coverage also allows us to trace the same line transition, CO(3–2), both at $\langle z \rangle \approx 0.49$ at 1.2 mm, and at $\langle z \rangle \approx 2.61$ at 3 mm. Because of the $\sim 16.2\times$ smaller volume and $\sim 7.7\times$ lower luminosity distance, we sample different ranges of the CO(3–2) luminosity function in the two redshift bins, with the low-redshift data mostly constraining the $L' < 10^9$ K km s^{-1} pc^2 regime and the high-redshift data pinning down the bright end at $L' > 2 \times 10^9$ K km s^{-1} pc^2. However, the difference in number density throughout the observed range strongly points towards an evolution of the CO(3–2) luminosity function between $z \sim 2.6$ and $z \sim 0.5$. This is even clearer once we compare the observed CO LFs with the empirical predictions based on the *Herschel* IR LFs from Vallini et al. (2016) shown in Figure 5.8. The *Herschel* IR LFs were scaled via an empirical relation of the form: $\log L'/(\mathrm{K\,km\,s^{-1}\,pc^2}) = 0.54 + 0.81 \log L_{\mathrm{IR}}/L_\odot$ (Sargent et al., 2014). The observed CO LF at $z \sim 0.5$ appears to sample just above the expected knee of the CO LFs. The observed CO(3–2) LF at $z \sim 2.6$ is in good agreement with the prediction for $z \sim 2$ around the expected
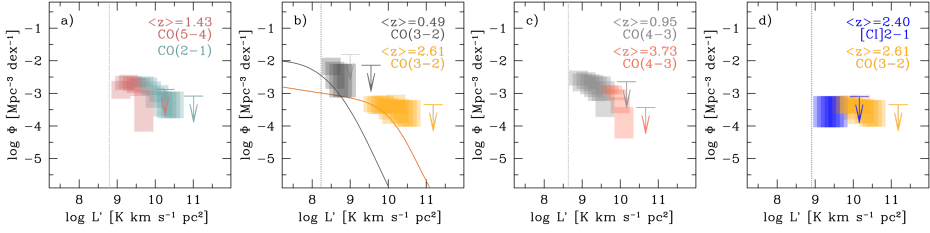
Figure 5.8: Comparison between CO and $[\text{C I}]_{2-1}$ luminosity functions. (a) The CO(2–1) (grey blue) and CO(5–4) (dark red) luminosity functions in the common redshift range around $\langle z \rangle = 1.43$. The CO(2–1) luminosity function appears in systematic excess with respect to the CO(5–4), hinting at generally subthermalized conditions ($r_{52} < 0.3$, see text for details). (b) The CO(3–2) luminosity functions observed at 3 mm and 1.2 mm at $\langle z \rangle = 2.61$ and $\langle z \rangle = 0.49$, respectively. For comparison, the empirical predictions of the CO(3–2) luminosity functions based on *Herschel* IR luminosity functions by Vallini et al. (2016) are shown in grey ($z \sim 0$) and orange ($z \sim 2$) lines. The CO(3–2) LF appears to evolve from $z \sim 2.6$ to the present age. ASPECS data point to an evolution in the CO(3–2) luminosity function consistent with the empirical predictions, although the difference in the sampled luminosity ranges in the two redshift bins limits the robustness of this finding. (c) Similar to the previous panel, but for the CO(4–3) luminosity functions observed at $z \sim 0.95$ at 1.2 mm and at $z \sim 3.7$ at 3 mm. (d) Comparison between the $[\text{C I}]_{2-1}$ and CO(3–2) luminosity functions at $z \sim 2.5$. We find an offset of $\gtrsim 0.5$ dex between the two luminosity functions, broadly in agreement with similar ratios between the two line luminosities reported in the literature from studies of individual sources (see § 5.4.2).

knee, and it lies >2 dex higher (in terms of number density) than the low-z predictions for $L' \sim 10^{10}$ K km s^{-1} pc^2. This result provides further, direct support to an evolution in the CO LFs, and therefore in gas content of galaxies, in this case irrespective of uncertainties in the CO excitation. We also show the comparison between the CO(4–3) LFs observed at $z \sim 0.95$ at 1.2 mm and $z \sim 3.7$ at 3 mm. A similar LF evolution might also be present in CO(4–3), but the available data do not allow us to exclude a non-evolving scenario.

5.4.2 [C I] and [C II] luminosity functions

In Figure 5.7, we also show the observed constraints on the $[\text{C I}]_{1-0}$ LF at $\langle z \rangle = 1.08$, on the $[\text{C I}]_{2-1}$ LF at $\langle z \rangle = 2.40$, and on the [C II] LF at $\langle z \rangle = 6.94$ from ASPECS 1.2 mm. With the exception of the strong $[\text{C I}]_{2-1}$ detection associated with the galaxy ASPECS LP 1mm.C01 (Boogaard et al., 2020; Aravena et al., 2020), only relatively low fidelity candidates are consistent with being [C I] or [C II] transitions. We further explore ASPECS contraints on the [C II] LF in B. Uzgil, et al. (in prep.).

Figure 5.8 shows the comparison between the $[\text{C I}]_{2-1}$ LF from our 1.2 mm cube, and the CO(3–2) LF from the ASPECS LP 3 mm. The two LFs probe roughly the same redshift range, so the comparison of the two LFs yields an insight on the average physical conditions in the ISM of the detected galaxies. We find a global shift of $\gtrsim 0.5$ dex between the two LFs, which is roughly consistent with the median ratio of 0.69 ± 0.16 dex for $[\text{C I}]_{2-1}/\text{CO(3–2)}$ reported in targeted observations of SMGs and quasar host galaxies at $z = 2 - 6$ in Walter et al. (2011).

For comparison, Jiao et al. (2017) find a ratio of 0.9 dex in local ULIRGs.

We refer to Boogaard et al. (2020) for a more detailed discussion of the astrophysical implication of the observed CO to [C I] line ratios, and to B. Uzgil, et al. (in prep.) for a further exploration of the upper limits on the [C II] LF.

5.4.3 ρ_{H_2} vs redshift

We use the combined ASPECS data to infer the cosmic-averaged molecular gas density of galaxies, ρ_{H_2}, as a function of cosmic time (see § 5.3.5). Compared to previous incarnations of our analysis (e.g., Walter et al., 2014; Decarli et al., 2016a, 2019), we here adopt the updated constraints on the CO excitation from Boogaard et al. (2020), which also includes the VLASPECS results (Riechers et al., 2020). Our analysis yields a nearly continuous sampling of $\rho_{H_2}(z)$ from $z \approx 0$ to $z \sim 4.5$ in a self-consistent manner. The ASPECS data show a smooth increase of $\rho_{H_2}(z)$ from early cosmic time up to $z \sim 1.5$, followed by a $\sim 6\times$ decline to the present day (see Figure 5.9 and Table 5.2). The new excitation correction (Boogaard et al., 2020) brings the $\rho_{H_2}(z)$ constraints from CO into excellent agreement with our dust-based measurements from ASPECS (Magnelli et al., 2020). The ρ_{H_2} constraints at $z \lesssim 0.5$ from ASPECS are rather loose, as a result of the small volume probed (see § 5.B).

We note that the results shown in Figure 5.9 are based on a constant α_{CO} or gas-to-dust ratio. The arguments presented in § 5.3.4 for a Galactic value may not be valid at $z \gtrsim 3$, where direct constraints on the metallicity of typical CO- and dust-emitting galaxies lack. A lower metallicity would imply a higher α_{CO} and gas-to-dust ratio, yielding higher ρ_{H_2} estimates.

We also derive [C I]-based estimates of $\rho_{H_2}(z)$ (see Table 5.2). The two [C I]-based estimates at $z \sim 1$ and $z \sim 2.5$ appear lower by a factor $\sim 5\times$ and $\sim 2\times$, respectively, compared to the corresponding CO-based estimates. This discrepancy is likely due to sensitivity limitations, and highlights the challenge of using [C I] as molecular gas tracer of the bulk of the galaxy population at high redshift (for dedicated [C I] studies in main sequence galaxies at high redshift, see, e.g., Valentino et al., 2018; Valentino et al., 2020b).

In Figure 5.9 we place the ASPECS measures of $\rho_{H_2}(z)$ in the context of similar investigations in the literature. Our new measurements, listed in Table 5.2, improve and expand on the results from previous molecular scans using the Plateau de Bure Interferometer (Walter et al., 2014), the VLA (Riechers et al., 2019), and ALMA (Decarli et al., 2016a, 2019), as well as the constraints from field sources in the PHIBSS data (Lenkić et al., 2020), and from calibrator fields in the ALMACAL survey (Klitsch et al., 2019). Our comparison also includes dust-based $\rho_{H_2}(z)$ measurements from Scoville et al. (2017), Liu et al. (2019), and from ASPECS (Magnelli et al., 2020). Overall, the molecular gas constraints from volume-limited surveys agree within the uncertainties over $\sim 90\%$ of the cosmic history. The general agreement in these results, based on different fields, suggests that the impact of cosmic variance and of systematics is modest. In § 5.B we quantitatively assess its role within our dataset. The studies by Scoville et al. (2017) and Liu et al. (2019) find a qualitatively similar evolution of $\rho_{H_2}(z)$, although with different normalizations. These ρ_{H_2} estimates rely on different assumptions of stellar mass functions, functional form of the main sequence, gas fractions, internal calibrations, and integration limits. Homogenizing these is beyond the scope of the present work, therefore we here only show their 'bona fide' estimates as published.
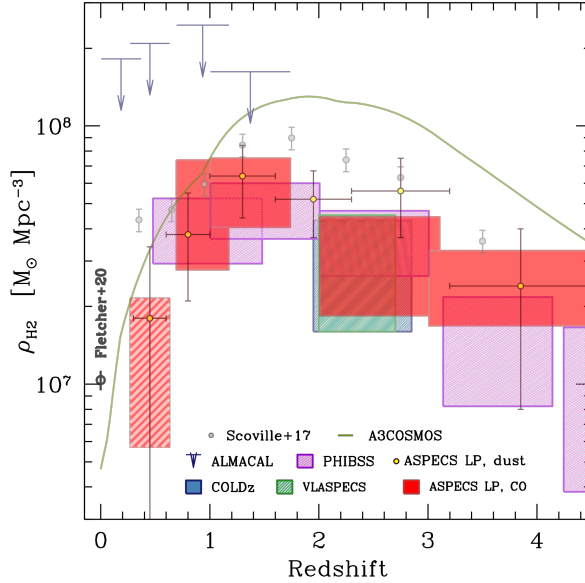
Figure 5.9: The evolution of the cosmic molecular gas density, $\rho_{H_2}(z)$, from ASPECS LP compared to similar studies in the literature: CO-based measurements from VLASPECS (Riechers et al., 2020), COLDz (Riechers et al., 2019), PHIBSS fields (Lenkić et al., 2020), ALMACAL (Klitsch et al., 2019); and dust-based measurements from ASPECS (Magnelli et al., 2020), A3COSMOS (Liu et al., 2019), and from Scoville et al. (2017, see their footnote 2). The $\rho_{H_2}(z = 0)$ measurement by Fletcher et al. (2020) is also shown for reference. All of the uncertainties are shown at 1σ significance. The ASPECS LP constraints at $z \lesssim 0.5$ are shaded to highlight the non-negligible impact of cosmic variance at these redshifts. The available datasets all point towards a steep decrease in ρ_{H_2} from cosmic noon to the local universe preceded by a smooth increase from higher redshift. Different surveys targeting different regions of the sky appear to find the same trend, implying that cosmic variance does not dominate the results (see § 5.B).

The observed evolution of ρ_{H_2} appears to mimic the history of the cosmic star formation rate density, ρ_{SFR} (see, e.g., Madau & Dickinson, 2014). The ratio between ρ_{H_2} and ρ_{SFR} results in a volume-average of the "depletion time" $\langle t_{dep} \rangle$, i.e., the timescale required for galaxies to deplete their reservoirs of molecular gas, if star formation continues at the current rate, and there is no further gas accretion or outflows. Our results hint to a relatively constant $\langle t_{dep} \rangle$. In Walter et al. (2020) we explore the astrophysical implications of this result in the context of galaxy evolution.

5.5   Conclusions

We present the ultimate CO luminosity functions from the ASPECS large program, and the resulting constraints for the cosmic evolution of the molecular gas density. The main conclusions of this study of the molecular and atomic line emission in ASPECS LP are as follows.

i. The line flux distributions due to various CO and neutral/ionized carbon lines in our analysis show that roughly 80% of the line flux at 3 mm is associated with CO(2–1) or CO(3–2) at the age of cosmic noon, and 60% of the line flux at 1.2 mm is due to intermediate-J CO transition ($J_{\rm up} = 3 - 6$) at $z \lesssim 2$. Higher-J CO transitions are negligible at 3 mm but account for 25% of the total line flux at 1.2 mm. Neutral carbon contributes to $\sim$ 12% of the integrated line flux at 1.2 mm. Finally, singly-ionized carbon [C II] at $6 \lesssim z \lesssim 8$ accounts for < 1% of the line flux at 1.2 mm. This result poses a major challenge for intensity mapping experiments targeting [C II] at the end of the epoch of reionization, as the expected line foreground is two orders of magnitudes stronger (in terms of total flux in lines) than the [C II] signal.

ii. The CO luminosity functions probed at 1.2 mm evolve as a function of redshift, with a decrease in the number density at a given line luminosity (in units of L'). This implies substantially subthermal excitation in galaxies throughout the last $\sim$10 Gyr of cosmic history.

iii. The direct comparison between the luminosity functions for the same CO transition seen in the 1.2 mm and 3 mm cubes of the ASPECS LP reinforces the idea that the typical galaxy at $z \approx 1.43$ shows subthermalized molecular gas emission, and that there is a significant evolution in the luminosity function for CO(2–1) takes place between $z \sim 2.8$ and $z \sim 0.5$ irrespective of any CO excitation assumption. A comparison between the [C I]$_{2-1}$ and CO(3–2) luminosity functions in the redshift range $z \sim 2.5$ suggests that the line ratio is in line with the values reported for IR-bright galaxies in targeted studies.

iv. The cosmic density of molecular gas in galaxies, $\rho_{\rm H_2}$, smoothly increases from early cosmic time up $z \sim 2 - 3$, followed by a factor $\sim$ 6 drop to the present age. This is in qualitative agreement with the cosmic SFR density, suggesting that the depletion time of galaxies is approximately constant in redshift once averaged over the galaxy population.

v. Modeling and the comparison with similar surveys suggest that cosmic variance does not play a dominant role in our estimates of $\rho_{\rm H_2}$ at $z \gtrsim 0.5$.

The emerging consensus on the evolution of $\rho_{\rm H_2}$ is the result of many hundreds of hours of integration with PdBI/NOEMA, VLA, and ALMA. Using these facilities to significantly expand on the latest campaigns is still possible, but observationally expensive. Future upgrades in the capabilities of available instruments (from the forthcoming completion of NOEMA, to the

plans outlined in the ALMA 2030 Roadmap, Carpenter et al. 2020, and in the next generation VLA white books, Murphy et al. 2018) are required in order to make the next transformational step in this field.

Acknowledgements

Facilities: ALMA

Authorship statement

This chapter presents and discusses the main result from ASPECS: the cosmic density of molecular gas. The central analysis of ASPECS was conducted in close collaboration by a small core team of authors, who each lead part of a series of interrelated papers that were published simultaneously in The Astrophysical Journal (including chapter 4). The lead author of this chapter is R. Decarli, who was in charge of conducting the analysis and writing the manuscript. The main contributions from L. A. Boogaard concern the detailed assessment of the high-fidelity lines, the analysis of the line flux distributions and associated tests involving the lines without counterpart and their impact on the cosmic molecular gas density, the adopted CO excitation, and the discussion of the intercomparison of the luminosity functions of carbon monoxide and atomic carbon, as well as reviewing and discussing the manuscript.

Appendix 5.A   Tabulated luminosity functions

Table 5.3 and Table 5.4 list the ASPECS constraints on the luminosity functions of CO, [C I] and [C II].

Table 5.3: Luminosity functions of the observed CO transitions.

log L' (K km s^{-1} pc^2)	log Φ (dex^{-1} Mpc^{-3})	log L' (K km s^{-1} pc^2)	log Φ (dex^{-1} Mpc^{-3})	log L' (K km s^{-1} pc^2)	log Φ (dex^{-1} Mpc^{-3})
(1)	(2)	(3)	(4)	(5)	(6)
CO(1–0), 3 mm		CO(3–2), 1.2 mm		CO(7–6), 1.2 mm	
8.5	< -1.38	8.5	$-2.44\ -1.91$	9.2	$-3.91\ -3.02$
8.6	< -1.38	8.6	$-2.86\ -2.03$	9.3	$-3.57\ -2.89$
8.7	< -1.38	8.7	$-3.12\ -2.09$	9.4	$-3.57\ -2.89$
8.8	< -1.38	8.8	$-3.12\ -2.09$	9.5	$-3.60\ -2.91$
8.9	< -1.38	8.9	$-3.12\ -2.09$	9.6	$-3.76\ -2.96$
9.0	< -1.40	9.0	< -1.81	9.7	$-4.34\ -3.11$
CO(2–1), 3 mm		CO(4–3), 1.2 mm		CO(8–6), 1.2 mm	
9.5	$-2.87\ -2.53$	8.9	$-2.76\ -2.30$	9.2	< -2.74
9.6	$-2.88\ -2.53$	9.0	$-2.94\ -2.39$	9.3	< -2.74
9.7	$-2.80\ -2.48$	9.1	$-2.87\ -2.35$	9.4	$-3.83\ -3.03$
9.8	$-2.85\ -2.51$	9.2	$-3.03\ -2.41$	9.5	$-3.83\ -3.03$
9.9	$-3.05\ -2.63$	9.3	$-3.11\ -2.44$	9.6	$-4.45\ -3.16$
10.0	$-3.44\ -2.83$	9.4	$-3.23\ -2.48$	9.7	$-4.45\ -3.16$
10.1	$-3.27\ -2.75$	9.5	$-3.23\ -2.48$	9.8	$-4.45\ -3.16$
10.2	$-3.71\ -2.93$	9.6	$-3.72\ -2.62$		
10.3	$-3.76\ -2.95$				
10.4	$-3.76\ -2.95$				
10.5	$-3.76\ -2.95$				
CO(3–2), 3 mm		CO(5–4), 1.2 mm		CO(9–8), 1.2 mm	
9.6	$-3.58\ -3.08$	9.1	$-3.16\ -2.62$	9.2	$-3.83\ -3.08$
9.7	$-3.63\ -3.09$	9.2	$-2.90\ -2.46$	9.3	$-3.93\ -3.12$
9.8	$-3.63\ -3.07$	9.3	$-2.86\ -2.44$	9.4	$-4.00\ -3.14$
9.9	$-3.62\ -3.07$	9.4	$-2.93\ -2.47$	9.5	< -2.78
10.0	$-3.80\ -3.13$	9.5	$-2.99\ -2.51$	9.6	< -2.87
10.1	$-3.94\ -3.19$	9.6	$-3.08\ -2.55$		
10.2	$-3.60\ -3.04$	9.7	$-4.17\ -2.89$		
10.3	$-3.91\ -3.17$				
10.4	$-4.02\ -3.21$				
10.5	$-4.02\ -3.21$				
10.6	$-4.02\ -3.21$				
CO(4–3), 3 mm		CO(6–5), 1.2 mm		CO(10–9), 1.2 mm	
9.7	$-3.01\ -2.75$	9.2	$-3.05\ -2.60$	9.2	< -2.80
9.8	$-3.03\ -2.77$	9.3	$-3.04\ -2.60$	9.3	< -2.80
9.9	$-3.21\ -2.88$	9.4	$-2.99\ -2.57$	9.4	< -2.84
10.0	$-3.61\ -3.12$	9.5	$-3.20\ -2.68$	9.5	< -2.86
10.1	$-4.38\ -3.42$	9.6	$-3.69\ -2.89$	9.6	< -2.86
10.2	< -3.09	9.7	$-3.92\ -2.95$		
		9.8	$-4.31\ -3.02$		

Notes. (Columns: 1, 3, 5) Luminosity bin center; each bin is 0.5 dex wide. (Columns: 2, 4, 6) minimum and maximum values of the luminosity function confidence levels at 1σ, or 3σ upper limits on the luminosity functions.

Table 5.4: Luminosity functions of the observed [C I] and [C II] lines.

log L' (K km s^{-1} pc^2) (1)	log Φ (dex^{-1} Mpc^{-3}) (2)	log L' (K km s^{-1} pc^2) (3)	log Φ (dex^{-1} Mpc^{-3}) (4)
[C I]$_{1-0}$, 3 mm		[C I]$_{2-1}$, 1.2 mm	
9.6	< -3.10	9.2	$-4.04\ -3.08$
9.7	< -3.07	9.3	$-4.04\ -3.08$
9.8	< -3.07	9.4	$-4.04\ -3.08$
9.9	< -3.08	9.5	$-4.04\ -3.08$
10.0	< -3.11	9.6	$-4.04\ -3.08$
10.1	< -3.11		
[C I]$_{1-0}$, 1.2 mm		[C II], 1.2 mm	
9.0	$-3.32\ -2.63$	9.1	< -2.95
9.1	$-3.28\ -2.61$	9.2	< -2.95
9.2	$-3.64\ -2.73$	9.3	< -2.95
9.3	< -2.38	9.4	< -2.95
9.4	< -2.38	9.5	< -2.97

Notes. (Columns: 1, 3) Luminosity bin center; each bin is 0.5 dex wide. (Columns: 2, 4) minimum and maximum values of the luminosity function confidence levels at 1σ, or 3σ upper limits on the luminosity functions.

Appendix 5.B   Cosmic variance

A critical limitation of pencil-beam surveys such as ASPECS is the impact of cosmic variance. Noticeably, a large fraction of the galaxies detected in CO(2–1) emission in ASPECS LP 3 mm belongs to a large overdensity at $z \approx 1.09$ (see Boogaard et al., 2019). Here we quantify how the clustering of sources impact our results. The expected number of galaxies in a volume-limited survey is:

$$N = \int_{V_1} \int_{V_2} (1 + \xi)\, n_1 n_2\, dV_1\, dV_2 \tag{5.7}$$

where n_i is the number density of galaxies, obtained by integrating the luminosity (or mass) function of galaxies down to the detection threshold of the survey, V_i is the survey volume, and ξ is the 3D 2-points correlation function, which accounts for the excess of galaxy counts compared to the average field due to galaxy clustering. In the linear clustering regime, ξ is often modeled as a power-law: $\xi(r) = (r/r_0)^{-\gamma}$. The variance on the expected numbers, Var[N], is usually referred to as cosmic variance. It comprizes of a Poissonian term, and a term due to the variations in the number counts due to clustering:

$$\sigma_v^2 = \frac{\langle N^2 \rangle - \langle N \rangle^2 - \langle N \rangle}{\langle N \rangle^2} = \frac{1}{V^2} \int_{V_1} \int_{V_2} \xi\, dV_1\, dV_2 \tag{5.8}$$
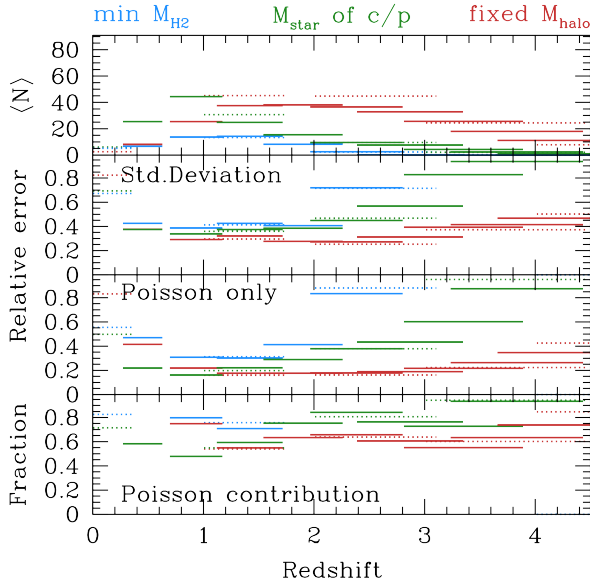
Figure 5.10: Impact of cosmic variance on the expected number counts of galaxies in our survey, based on the models presented in Popping et al. (2020), as a function of redshift. Blue, green, and red lines show galaxies selected based on the predicted CO luminosity (via the simulated H_2 mass), on the stellar mass of their optical/near-infrared counterparts, and on the halo mass, respectively (see text for details). The *top panel* shows the average number of galaxies in each redshift bin probed with ASPECS LP 1.2 mm (solid lines) and 3 mm (dotted lines). The *second panel* shows the root square of the total cosmic variance. The *third panel* shows the Poissonian term alone. Finally, the *bottom panel* shows the fraction of the standard deviation that is due to Poisson. We find that the Poisson contribution dominates the cosmic variance (> 50% of the standard deviation) at any redshift, irrespective of the selection function. This implies that the impact of clustering (i.e., the non-Poissonian component of the cosmic variance) is small, and often negligible in ASPECS.

As discussed in Decarli et al. (2016a) and Decarli et al. (2019), the Poissonian uncertainties are accounted for in the construction of the CO luminosity functions and in our estimates of ρ_{H_2}. The clustering term in Equation 5.8 implies that, even in presence of large source counts, field-to-field variations are expected due to large-scale structures and clustering. This might introduce a systematic bias in the estimates of LFs based on datasets centered on preselected targets (see also Loiacono et al., 2020). Here we quantify how our results depend on the choice of the targeted region.

Directly solving the integral in Equation 5.8 would require assumptions on the clustering of CO-bright sources, for which no direct observational constraint is available yet. An alternative and commonly-adopted approach is to rely on theoretical models of galaxy formation to create multiple realizations of galaxy populations in various volume samplings. Cosmic variance is then directly computed using the actual variations of N. Here we follow the latter

method by capitalizing on data-driven simulations presented in Popping et al. (2020). From these simulations we create 100 samplings of the simulated box with a geometry matched to the ASPECS survey volume. We then apply different cuts on the galaxy samples to mimic the selection criteria of ASPECS (see below). Finally, we compute the average and variance in the number of selected galaxies from all the realizations. The variance is a combination of the intrinsic scatter due to the cosmic structures within the simulation, and of Poissonian scattering. The contribution of the latter is directly computed following Gehrels (1986), thus we can infer the impact of large-scale structures in the count rates used in our LFs.

The results of this analysis are presented in Figure 5.10, where we show the average number of galaxies, the standard deviation (i.e., the squared root of the total variance in the number of galaxies), the Poissonian fluctuations, and the fraction of the uncertainties that is attributed to Poissonian fluctuations. Concerning the selection function, for a given transition, ASPECS applies a selection based on the line flux. As this is not trivially derived in models (see extensive discussions in, e.g., Lagos et al., 2011; Popping et al., 2014, 2019), here we opt for three different approaches: First, we apply a simple, redshift independent cut in the dark matter halo mass, $M_{halo} > 10^{11.5}$ M$_\odot$. Then we consider a cut based on the minimum stellar mass of detected optical/near-infrared counterparts as a function of redshift. The threshold is $M_{star} > 10^{9.0}$ M$_\odot$ at $z \approx 0.5$, $M_{star} > 10^{9.7}$ M$_\odot$ at $z \approx 1.4$, $M_{star} > 10^{10.1}$ M$_\odot$ at $z \approx 2.4$, $M_{star} > 10^{10.3}$ M$_\odot$ at $z \approx 3.5$, at $M_{star} > 10^{10.5}$ M$_\odot$ at $z \approx 4.5$. Finally, we consider a cut based on the CO 5σ luminosity thresholds shown in Figure 5.1, using the predicted CO luminosity in models, based on the simulated H$_2$ mass, under the same r_{J1} and α_{CO} assumptions as used elsewhere in this work (see § 5.3.4). We find that the number of galaxies we expect to detect is < 15 in each redshift bin for the CO luminosity cut, while the stellar mass cut at the halo mass cut yield larger numbers of expected galaxies (up to ~ 50 around cosmic noon). However, even in these cases, Poissonian uncertainties appear to dominate the total error budget, i.e., the Poisson contribution accounts for $> 50\%$ of the standard deviation in the number of galaxies at any redshift, irrespective of the selection function. Variance purely due to the large-scale structure in the universe (second panel from the top in Figure 5.10) plays a significant role only at $z \lesssim 0.5$ (in all cases) and $z \gtrsim 3 - 4$ (depending on the adopted the adopted selection cut. The overall low impact of cosmic variance is likely to be attributed to the peculiar pencil beam geometry of the survey, with the line-of-sight dimension stretching over ~ 1000 Mpc in most redshift bins. The Poissonian fluctuations are already accounted for in the LFs and estimates of $\rho_{H_2}(z)$. The remainder term, due to the clustering of sources, is small in the redshift range of interest, its actual value strongly depends on the (unknown) reliability of our forward-modeling of the selection function. Therefore, we opt not to include this further term into our estimates of the uncertainties. In support to the negligible contribution of cosmic variance, Magnelli et al. (2020) and Bouwens et al. (2020) find an excellent match between the stellar mass functions and cosmic SFR density in the ASPECS footprint and the ones inferred in the literature from much wider regions in different (physically disconnected) fields at any $z \gtrsim 0.5$.
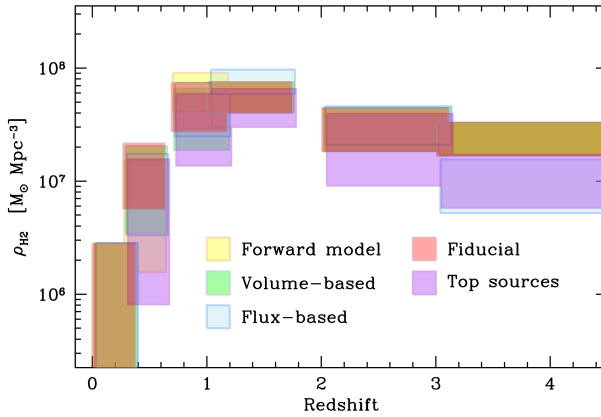
Figure 5.11: The evolution of the molecular gas cosmic density in galaxies as a function of redshift, shown under different treatments of the line candidates without a counterpart. Red boxes: our bona-fide constraints, as shown in Figure 5.9. Green boxes: the probability distribution of line identification scales with the sampled volume in each transition, for both ASPECS bands. Yellow boxes: the probability distribution of line identification scales as the volume for 3 mm transitions, and as the predicted number of detections assuming the corresponding CO LFs from 3 mm at similar redshifts, and the large velocity gradient modeling of the CO spectral energy distribution from Boogaard et al. (2020). Blue boxes: the probability distribution scales as the observed flux distributions shown in Figure 5.5. Purple boxes: Constraints on ρ_{H_2} based exclusively on the sources detected in the 1.2 mm dust continuum.

Appendix 5.C   Identification of line candidates without near-infrared counterparts

Here we explore how our treatment of the line candidates without a counterpart affects our results on the molecular gas content in the universe, $\rho_{H_2}(z)$. The expected number of lines from a specific transition is given by the integral over the corresponding above the luminosity limit set in Figure 5.1, scaled for the cosmological volume sampled in such transition. In addition, the lack of a counterpart in our multiwavelength catalog implies an additional, unknown selection function that favors high-redshift scenarios. The modest information content in the data concerning the actual redshift of line candidates without a counterpart implies that the posterior distributions might be affected by our prior assumptions. Hence, we test how different options affect our final results.

Beside our fiducial approach described in § 5.3.5, we consider four scenarios: 1) We assume that the probability distribution of line identification is proportional to volume; 2) We assume the same volume-based argument at 3 mm, and infer expected LFs (and hence, expected number of sources) for 1.2 mm transitions based on the CO LFs from Saintonge et al. (2017) (extrapolated to $z \sim 0.5$) and from Decarli et al. (2019) (at $z \gtrsim 0.9$), paired with the large velocity gradient analysis on individual ASPECS sources from Boogaard et al. (2020); 3) For both bands we assume that the probability distribution scales according to the flux

Table 5.5: The cosmic molecular gas density (mass of molecular gas in galaxies per cosmological volume) as constrained by ASPECS under different methods to identify line candidates without counterparts (see text for details).

Redshift	log ρ_{H_2} (M$_\odot$ Mpc^{-3})			
	Forward model	Volume-based	Flux-based	Top sources
(1)	(2)	(3)	(4)	(5)
0.003–0.369	5.171–6.449	5.171–6.449	5.177–6.453	
0.271–0.631	6.196–7.184	6.537–7.312	6.522–7.240	5.911–7.194
0.695–1.174	7.617–7.957	7.278–7.819	7.398–7.871	7.138–7.772
1.006–1.738	7.608–7.874	7.608–7.874	7.769–7.984	7.481–7.816
2.008–3.107	7.266–7.647	7.266–7.647	7.322–7.663	6.961–7.595
3.011–4.475	7.227–7.517	7.227–7.517	6.720–7.190	6.766–7.235

Notes. The quoted values refer to the 1σ upper- and lower condifence boundaries.

distribution of line candidates with a counterpart (see Figure 5.5); 4) Finally, we restrict our analysis to lines with a 1.2 mm continuum counterpart (see González-López et al., 2020; Aravena et al., 2020). These different approaches have their strengths and drawbacks. The volume-based arguments use the least prior information, but they do not account for the different luminosity limits and for the evolution of the LFs, nor for the intrinsic ratios of line luminosities. The flux-based method has the advantage of resulting in a realistic distribution of the line fluxes for sources without a counterpart, but inherently assumes that the sources with and without a counterpart share a similar redshift and flux distribution, which is unlikely. The forward-modeling method has the advantage of exploiting the information available at 3 mm and from local studies to constrain the 1.2 mm LFs, but it relies on extrapolation of observed LFs in different redshift bins, and is partially circular, in that the excitation constraints are based on the same 1.2 mm data. Finally, limiting the analysis to secure sources provides us with a robust lower limit, but this approach does not fully capitalize on the signal present in the data.

Figure 5.11 compares the $\rho_{H_2}(z)$ evolution that results from each assumption (see also Table 5.5). To first order, the ρ_{H_2} evolution is unaffected by our treatment of the sources without a counterpart in the catalog. The spread between the ρ_{H_2} estimates is most prominent at $z \lesssim 0.5$ as a result of low number statistics. Discrepancies are always well within the uncertainties. The main offset comes from restricting our analysis to the secure sources with a 1.2 mm dust continuum, which typically results in a $\sim 1.5\times$ underestimate of ρ_{H_2}.